ACS Catalysis

Research Article

Cite This: *ACS Catal.* 2019, 9, 8433−8442

pubs.acs.org/acscatalysis

Electrocatalytic Production of H_2O_2 by Selective Oxygen Reduction Using Earth-Abundant Cobalt Pyrite (CoS_2)

Hongyuan Sheng,[†,∥] Eric D. Hermes,[†,∥] Xiaohua Yang,[†,‡,∥] Diwen Ying,[†,§] Aurora N. Janes,[†]
Wenjie Li,[†] J. R. Schmidt,[*,†] and Song Jin[*,†]

[†]Department of Chemistry, University of Wisconsin−Madison, 1101 University Avenue, Madison, Wisconsin 53706, United States

[‡]Key Laboratory of Ultrafine Materials of Ministry of Education, School of Materials Science and Engineering, East China University of Science and Technology, 130 Meilong Road, Shanghai 200237, China

[§]School of Environmental Science and Engineering, Shanghai Jiao Tong University, 800 Dongchuan Road, Shanghai 200240, China

Supporting Information

ABSTRACT: Decentralized on-site production of hydrogen peroxide (H_2O_2) relies on efficient, robust, and inexpensive electrocatalysts for the selective two-electron ($2e^-$) oxygen reduction reaction (ORR). Here, we combine computations and experiments to demonstrate that cobalt pyrite (CoS_2), an earth-abundant transition-metal compound, is both active and selective toward $2e^-$ ORR in the acidic solution. CoS_2 nanomaterials drop-casted on the rotating ring-disk electrode (RRDE) showed selective and efficient H_2O_2 formation in 0.05 M H_2SO_4 at high catalyst loadings, with their operational stability evaluated by structural and surface analyses. CoS_2 nanowires directly grown on the high-surface-area carbon fiber paper electrode boosted the overall performance of bulk ORR electrolysis and the H_2O_2 product was chemically quantified to yield a ~70% H_2O_2 selectivity at 0.5 V vs reversible hydrogen electrode (RHE), in good agreement with the RRDE results. Computations suggested the modest binding of OOH* adsorbate on the single Co site of CoS_2 and the kinetically disfavored O−O bond scission due to the lack of active site ensembles in the crystal structure, consistent with the experimentally observed activity and selectivity. CoS_2 also catalyzes $2e^-$ ORR with less activity and selectivity in the noncorrosive neutral solution. This work opens up the exploration of diverse earth-abundant transition-metal compounds in search of highly active and selective electrocatalysts for efficient H_2O_2 production.

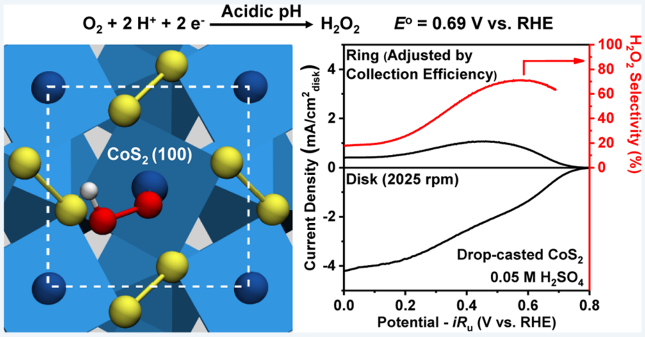

KEYWORDS: *selective electrocatalysis, oxygen reduction, hydrogen peroxide, earth-abundant, pyrite*

INTRODUCTION

Hydrogen peroxide (H_2O_2) is an efficient and environmentally benign oxidant with diverse industrial applications including pulp- and paper-bleaching, chemical synthesis, and wastewater treatment.[1,2] Commercial production of H_2O_2 (5.5 million tons per year in 2015) has been almost exclusively taking place through an indirect anthraquinone process that involves sequential hydrogenation (under H_2 gas) and autoxidation (in the air) of anthraquinone.[1,2] Direct chemical synthesis of H_2O_2 from H_2 and O_2 gases has also been explored, yet a very few noble metal alloy catalysts show satisfactory selectivity toward H_2O_2.[3−5] Both chemical approaches of H_2O_2 synthesis use large quantities of H_2 gas, which is both costly and energy intensive to obtain. Moreover, these centralized production methods require long-distance transportation of concentrated H_2O_2 to end-users with significant expenses and safety concerns. In fact, low concentrations of H_2O_2 are usually sufficient for most applications, which motivates sustainable on-site production and utilization of H_2O_2 in a decentralized manner.

In this context, direct H_2O_2 production via electrochemical, rather than chemical, reduction of O_2 eliminates the need for H_2 gas, allowing for not only reduction in both costs and energy consumption but also safer deployment in a modular and decentralized fashion. The electricity needed in electrochemical oxygen reduction reaction (ORR) can come from renewable solar and wind energy,[6] which are also decentralized and becoming more affordable. The major challenge here is to selectively reduce O_2 to H_2O_2 (vs H_2O) via a two-electron (vs four-electron) pathway. Recent developments of selective two-electron ($2e^-$) ORR catalysts have been mostly focused on carbon materials[7−12] and noble metals.[13−19] In carbon materials, carbon defects[7−10] and heteroatom dopants[9,11] were exploited as the active sites for selective $2e^-$ ORR; however, they are sufficiently active only in the alkaline solution[8,11] where H_2O_2 is unstable,[1] and significant challenges

Received: June 17, 2019
Revised: July 28, 2019
Published: August 1, 2019

DOI: 10.1021/acscatal.9b02546
ACS Catal. 2019, 9, 8433−8442

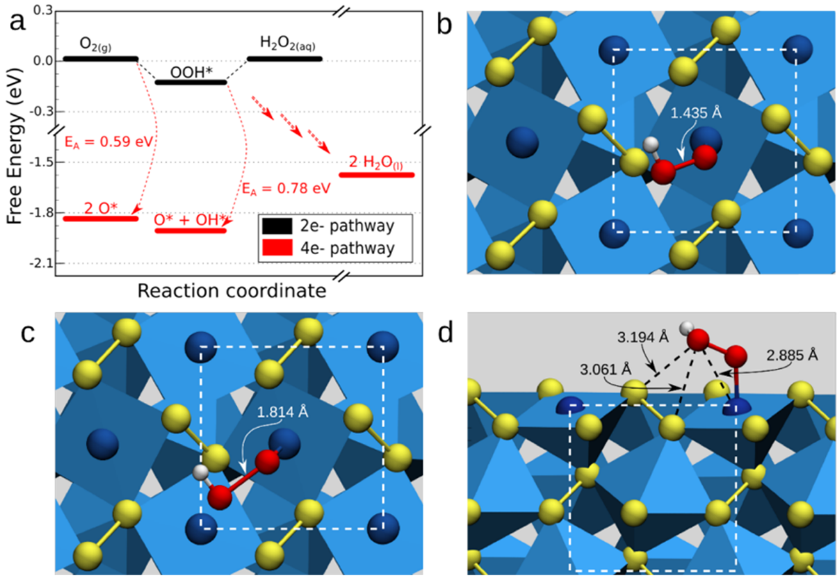

Figure 1. Computational modeling of ORR on the CoS_2 (100) surface. (a) Free energy diagram for both $2e^-$ and $4e^-$ ORR at the calculated standard equilibrium reduction potential of $2e^-$ ORR. (b) Top view of (b) the CoS_2 surface with adsorbed OOH* and (c) the transition state for OOH* scission. (d) Side view of the CoS_2 surface with adsorbed OOH*.

remain in the rational synthesis of defects and dopants with atomic precision. Selective $2e^-$ ORR over noble metals necessitates the isolation of active sites to suppress O−O bond scission by adjacent active sites and, thus, $4e^-$ ORR, which was realized by either dispersing active metals within inert matrices (e.g., Pd−Au,[13,14] Pt−Hg,[15] Pd−Hg[16]) or anchoring single metal atoms onto supports;[17−19] however, they involve expensive or sometimes toxic metals. Compared to noble metals, earth-abundant transition-metal compounds not only enable better isolation of active (metal) sites but also offer unique surface structural motifs with more diverse and controllable tunability, allowing for optimized adsorbate binding and, therefore, potentially enhanced activity and selectivity toward H_2O_2 production. In addition, as both acidic and alkaline solutions are corrosive, on-site production of H_2O_2 in the noncorrosive neutral solution is advantageous for practical wastewater treatment applications by avoiding the need for neutralization.

Here, we present a joint computational/experimental study to demonstrate that earth-abundant cobalt pyrite (CoS_2) is both active and selective toward $2e^-$ ORR in acidic and neutral solutions, with its catalytic performance in the acidic solution approaching those of the state-of-the-art catalysts containing noble and/or toxic metals. Chemical quantification of the H_2O_2 product electrogenerated on the CoS_2 catalyst from the bulk ORR electrolysis in the acidic solution further demonstrates the promise of this catalyst for practical applications. Computations reveal general mechanistic insights into the activity and selectivity of earth-abundant transition-metal compounds toward $2e^-$ ORR. This study opens up new directions in search of more active and selective electrocatalysts for efficient decentralized production of H_2O_2.

RESULTS AND DISCUSSION

Metallic pyrites have been known as versatile earth-abundant electrocatalysts toward hydrogen evolution, triiodide- and polysulfide-reduction,[20,21] which led us to consider metallic pyrites as possible $2e^-$ ORR electrocatalysts. Computational modeling of ORR was performed on the CoS_2 (100) surface using density functional theory (DFT) and the computational hydrogen electrode (CHE) approach.[22−26] The surface energy of the (100) facet (0.032 eV/Å^2) is considerably lower than those of the (110) or (111) facets (0.060 and 0.057 eV/Å^2, respectively) since the (100) surface preserves the disulfide (S_2^{2-}) dumbbells. As such, our initial computational work focuses on the thermodynamically most stable (100) facet, which is the most probable facet present in our experimental samples (see below) and also the simplest one to start with to generate mechanistic insights. The activity of CoS_2 toward $2e^-$ ORR is governed by the following proton-coupled electron transfer (PCET) steps,[23−25]

$$O_2 + * + (H^+ + e^-) \rightarrow OOH* \tag{1}$$

$$OOH* + (H^+ + e^-) \rightarrow H_2O_2 + * \tag{2}$$

where * is the unoccupied active site (Co site in CoS_2) and OOH* is the sole adsorbate for $2e^-$ ORR. The first PCET step, forming OOH*, is modestly exergonic ($\Delta G = -0.14$ eV) at the thermodynamic potential of $2e^-$ ORR (Figure 1a). The overpotential of $2e^-$ ORR on CoS_2 is, therefore, determined by the reduction of OOH* to H_2O_2 (only 0.14 eV uphill in free energy), making CoS_2 very active toward H_2O_2 formation. On the other hand, the selectivity of $2e^-$ vs $4e^-$ ORR is determined by the resistance to O−O bond scission,[23−25] forming O* and/or OH* as adsorbates for $4e^-$ ORR.

$$O_2 + 2* \rightarrow 2\,O* \tag{3}$$

$$OOH* + * \rightarrow O* + OH* \tag{4}$$

$$OOH* + (H^+ + e^-) \rightarrow O* + H_2O \tag{5}$$

The O−O bonds in adsorbed O_2 and OOH* can potentially be thermally cleaved onto adjacent active sites (eqs 3 and 4), but these processes exhibit substantial activation energy barriers on CoS_2 (0.59 and 0.78 eV, respectively). We find that the crucial O−O bond cleave process in OOH* happens preferentially via a binuclear pathway across two neighboring Co sites (barrier of 0.78 eV) rather than neighboring Co and S

DOI: 10.1021/acscatal.9b02546
ACS Catal. 2019, 9, 8433−8442

sites (0.84 eV), most likely due to the strong binding preference of O* to S and OH* to Co, respectively. Another possible pathway is the migration of OOH* onto S prior to dissociation; however, we can disregard this pathway because the energetics of this migration is less favorable than the binuclear dissociation barrier across neighboring Co sites. This is consistent with the established understandings on the molecular ORR catalyst cobalt porphyrins that (1) monomeric cobalt porphyrins usually catalyze $2e^-$ ORR and (2) cofacial dicobalt porphyrins catalyze $4e^-$ ORR.[27]

Focusing specifically on the key potential-determining step, OOH* cleavage is unlikely to compete with the rapid reduction of OOH* to H_2O_2 (eq 2). This observation lies in sharp contrast to close-packed metal surfaces, which, in turn, display minimal activation barriers for rapid OOH* scission (0.06, 0.16, and 0.06 eV on (111) facet of Pd, Pt, and Cu).[26] We hypothesize that such difference is associated with the absence of active ensemble sites in the crystal structure of CoS_2. The neighboring Co sites in CoS_2 are separated by 3.941 Å, whereas the minimum-energy configuration of OOH* has an O−O bond length of only 1.435 Å (Figure 1b). To reach the transition state for OOH* scission, the O−O bond in OOH* elongates considerably to 1.814 Å and becomes highly strained (Figure 1c), the CoS_2 also experiences significant lattice distortion with a shorter distance between neighboring Co sites (3.645 Å). In contrast, the transition state for OOH* scission on close-packed metal surfaces is much less distorted from the reactant geometry. In addition, O−O bond cleavage through reductive elimination of OOH* (eq 5) is also kinetically disfavored on CoS_2. Compared to most metal surfaces that interact closely with both oxygens in OOH*, only one of the oxygens in OOH* is in the immediate vicinity of the CoS_2 surface due to its isolated active sites (Figure 1d). As a result, PCET to the surface-bound oxygen on CoS_2 (leading to H_2O_2) likely dominates over that to the distant oxygen (yielding H_2O and O*), which requires through-space transfer (approximately 3 Å, see Figure 1d) or tunneling through the O−O bond. The addition of an empirical dispersion correction to these density functional results does not qualitatively alter this picture (Figure S1 in the Supporting Information).[28]

Our experimental results (see below) suggest that the operating catalyst surface appears to be unoxidized, and, thus, we do not expect a high surface coverage of O*. Nonetheless, we find that the binding energy of OOH* is fairly insensitive to the coverage of O* on S (its preferred binding site), with an adjacent O* altering the OOH* binding energy by only ~0.07 eV. We discount the buildup of OH* due to its presumed rapid reduction to water. Overall, our computational results suggest that $2e^-$ ORR is selectively initiated at low overpotential on the single Co site of CoS_2, while $4e^-$ ORR on CoS_2 is kinetically suppressed by the large spacing between neighboring Co sites.

To experimentally verify our computational predictions, we prepared CoS_2 nanomaterials via thermal sulfidation of hydrothermally synthesized cobalt hydroxide carbonate hydrate nanomaterials (Figure S2a).[21] Scanning electron microscopy (SEM) images of CoS_2 showed the nanowire morphology with surface roughness (Figure S2b). Powder X-ray diffraction (PXRD) (Figure S2c) and energy-dispersive X-ray spectroscopy (EDS) (Figure S3) confirmed the phase purity and elemental compositions of CoS_2. We systematically studied the catalytic activity and selectivity of the CoS_2 nanomaterials toward $2e^-$ ORR in both acidic (0.05 M H_2SO_4) and neutral (0.05 M Na_2SO_4) solutions using a rotating ring-disk electrode (RRDE) that consists of a glassy carbon (GC) disk surrounded by a Pt ring. The collection efficiency of the bare RRDE, calibrated with a reversible and fast ferri-/ferrocyanide redox couple when both ferricyanide reduction on the GC disk and ferrocyanide oxidation on the Pt ring are diffusion-limited, is 0.43 and is independent of the RRDE rotation rate (Figure S4). To determine ORR selectivity using this collection efficiency value, the Pt ring needs to drive fast H_2O_2 oxidation without triggering water oxidation.[29,30] This ring potential is usually set between 1.2 and 1.3 V vs reversible hydrogen electrode (RHE) regardless of the pH of the electrolyte.[31,32] We experimentally verified that 1.3 V vs RHE is an appropriate ring potential for both 0.05 M H_2SO_4 and 0.05 M Na_2SO_4 by performing ORR measurements and analyzing H_2O_2 selectivity of commercial Pt/C (a known $4e^-$ ORR catalyst[31]) and Vulcan carbon black (moderately selective toward $2e^-$ ORR but has a poor activity[11]), as shown in Figures S5 and S6.

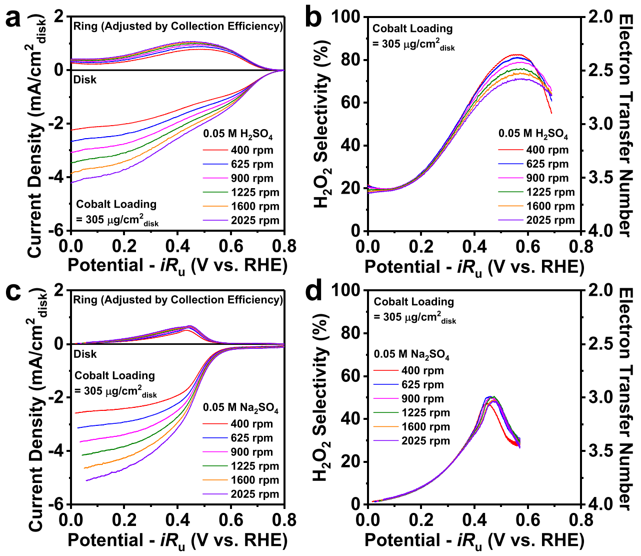

Figure 2. (a, c) RRDE measurements of drop-casted CoS_2 (cobalt loading = 305 $\mu g/cm_{disk}^2$) at different rotation rates and (b, d) the corresponding H_2O_2 selectivity in O_2-saturated (a, b) 0.05 M H_2SO_4 and (c, d) 0.05 M Na_2SO_4.

We then drop-casted CoS_2 nanomaterials on RRDE (cobalt loading = 305 $\mu g/cm_{disk}^2$) without carbon support and measured their intrinsic activity and selectivity toward $2e^-$ ORR in both acidic and neutral solutions without interference from carbon (Figure 2). The disk potential was set not to exceed 0.80 V vs RHE to prevent the anodic dissolution of CoS_2 via oxidation of sulfide to sulfate.[33,34] We note that, for the ease of directly visualizing the H_2O_2 selectivity from the RRDE voltammograms (Figure 2a,c), both the disk and the ring current densities are presented based on the geometric area of the disk electrode (0.126 cm^2), and the ring current density was further adjusted by collection efficiency. In 0.05 M H_2SO_4 (pH 1.26), the catalytic onset on CoS_2 was close to the thermodynamic potential of $2e^-$ ORR (0.69 V vs RHE). As the disk potential was swept negatively, the disk current density kept increasing, whereas the ring current density reached its maximum and then declined (Figure 2a), indicating that the optimal H_2O_2 production on CoS_2 in the acidic solution takes place at the low overpotential region. Nevertheless, the H_2O_2

selectivity peaked at 70−80% and remained above 50% over a wide potential range (above 0.35 V vs RHE, Figure 2b), suggesting that H_2O_2 is the primary ORR product on CoS_2 in the acidic solution before $4e^-$ ORR takes over at high overpotentials. We further performed the same RRDE measurement in 0.1 M $HClO_4$ (pH 1.02) to show that the ORR activity and selectivity of CoS_2 in the acidic solution are unaffected by the electrolyte anions (Figure S7a−d). The H_2O_2 selectivity of CoS_2 in 0.05 M H_2SO_4 (determined by the RRDE method) exhibits a slight dependence on the rotation rate (Figure 2b); such dependence, as documented in the RRDE theory and reported on other ORR catalysts, is characteristic of the ORR that has multiple parallel pathways.[29] To further confirm this, we examined the ORR on CoS_2 under a higher concentration of acid (0.5 M H_2SO_4, pH 0.35) and still observed such dependence (Figure S7e,f), suggesting that the local pH variation at the catalyst surface (which might be more severe in the more diluted acidic solution) is unlikely to be the cause of such dependence. Electrochemically active surface areas (ECSAs) of drop-casted CoS_2 in different acidic solutions were estimated by the double-layer capacitance (C_{dl}) measurements (Figure S8). In the neutral solution of 0.05 M Na_2SO_4 (pH 6.14), the catalytic onset on CoS_2 took place around 0.54 V vs RHE (150 mV overpotential for $2e^-$ ORR), both the ring current density (Figure 2c) and the H_2O_2 selectivity (below 50%, Figure 2d) were lower than those achieved in 0.05 M H_2SO_4. To explain the observed pH dependence of the H_2O_2 selectivity, we suggest that, in the neutral solution where proton concentration is sufficiently low, H_2O instead of H^+ becomes the major proton source involved in the ORR elementary steps (eqs 1−5) and, therefore, alters the catalytic mechanism and selectivity. Note that using unbuffered 0.05 M Na_2SO_4 as the neutral electrolyte, even though closer to the practical applications, has some limitations because the local pH at the catalyst surface could become more alkaline under ORR conditions and may vary across the potential sweep. We do not present experimental results of the ORR on CoS_2 in the alkaline solution because (1) H_2O_2 is known to be chemically less stable in the alkaline solution,[1] which we experimentally verified by observing a higher decomposition rate of nonstabilized H_2O_2 in the alkaline solution compared with that in the acidic solution, which is negligible over the time period of one week (Figure S9); (2) CoS_2 is not chemically stable in the alkaline solution under oxidative environments.[35] Overall, these results show that the electrocatalytic production of H_2O_2 on CoS_2 is quite efficient in the acidic solution and is feasible in the noncorrosive neutral solution.

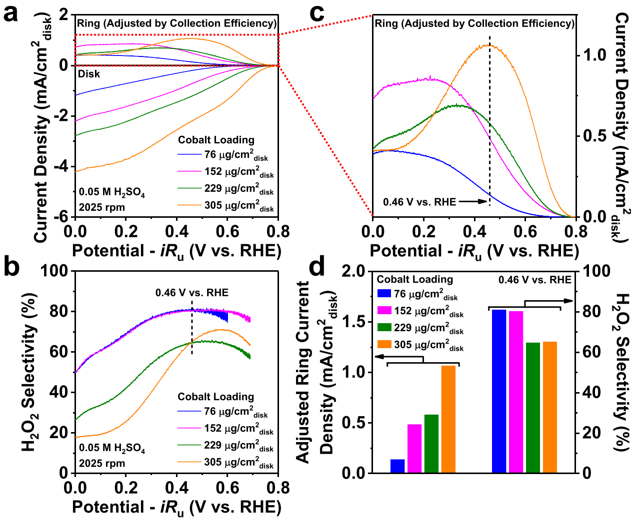

Figure 3. (a) RRDE measurements of drop-casted CoS_2 with various cobalt loadings at 2025 rpm in O_2-saturated 0.05 M H_2SO_4 (adapted from Figures 2a and S10). Comparisons of (b) the H_2O_2 selectivity and (c) the ring current density. Comparisons of the ring current density and the H_2O_2 selectivity at 0.46 V vs RHE are highlighted in (d).

To explore the optimal operating conditions of electrocatalytic H_2O_2 production on CoS_2 in the acidic solution, we investigated the influence of catalyst loadings on the ORR activity and selectivity of drop-casted CoS_2 in 0.05 M H_2SO_4 at 2025 rpm (Figures 3, S10 and Table S1). As the cobalt loading was gradually reduced from 305 to 76 $\mu g/cm_{disk}^2$, the disk current density became smaller (Figure 3a) due to the lower amount of catalytic active sites; however, the H_2O_2 selectivity at high overpotentials clearly improved (Figure 3b). Interestingly, the two lowest cobalt loadings (76 and 152 ug/cm_{disk}^2) exhibited essentially the same H_2O_2 selectivity over the entire potential range. We hypothesize that (1) when the catalyst loading is below a certain critical value, the catalytic active sites are likely to be completely saturated by the steady-state O_2 flux at the RRDE surface, yielding the nearly identical H_2O_2 selectivity profiles; (2) as the catalyst loadings go beyond this critical value, the excess catalytic active sites that are not saturated by the O_2 flux might trigger side reactions ($4e^-$ ORR, H_2O_2 reduction and/or decomposition) at high overpotentials that reduce the H_2O_2 selectivity. Nevertheless, at the more important low overpotential region, the high selectivity of H_2O_2 formation on CoS_2 is less affected by catalyst loadings (Figure 3b), and the ring current density still increases with higher catalyst loadings (Figure 3c). This is particularly the case at 0.46 V vs RHE where the maximum ring current density was achieved at the highest cobalt loading (Figure 3d). Since the practical focus of electrocatalytic H_2O_2 production is to boost the overall H_2O_2 yield at small overpotentials, these results suggest that a high catalyst loading of CoS_2 should be used for the best overall performance of electrocatalytic H_2O_2 production in the acidic solution. The catalyst loading effects of drop-casted CoS_2 were also studied in 0.05 M Na_2SO_4 (Figure S11). ECSAs of drop-casted CoS_2 in both 0.05 M H_2SO_4 and 0.05 M Na_2SO_4 systematically increased at higher catalyst loadings (Figure S12).

To compare the catalytic performance of CoS_2 with other reported ORR electrocatalysts for H_2O_2 production in the acidic solution based on RRDE measurements, we extracted the kinetic current density for H_2O_2 production ($j_{k,peroxide}$, see definition in the Supporting Information) from the RRDE voltammograms of CoS_2 (cobalt loading = 305 $\mu g/cm_{disk}^2$) in 0.05 M H_2SO_4 (shown in Figure 2a) by correcting the ring current density (i.e., the hydrogen peroxide current density, $j_{peroxide}$, see definition in the Supporting Information) for mass-transport loss (see Figure S13 and Table S2 for details). From the point of view of end applications, $j_{k,peroxide}$ is the most relevant parameter to reflect how much H_2O_2 product can be generated on the catalyst electrode (i.e., the actual yield of the H_2O_2 product) at a given potential without mass-transport limitation. We note that $j_{k,peroxide}$ can be affected by the catalyst loading and the catalyst surface area; therefore, we normalized $j_{k,peroxide}$ to the geometric area of the disk electrode for the ease of directly comparing the overall electrode performances of

CoS_2 and other reported ORR catalysts (with their RRDE electrode information summarized in Table S3). The comparison of the mass-transport-corrected Tafel plots of $j_{k,peroxide}$ in the acidic solution (Figure 4) clearly shows that, at the most important low overpotential region, the overall electrode performance of H_2O_2 production on the CoS_2 catalyst is approaching those on the state-of-the-art catalysts based on noble and/or toxic metals.

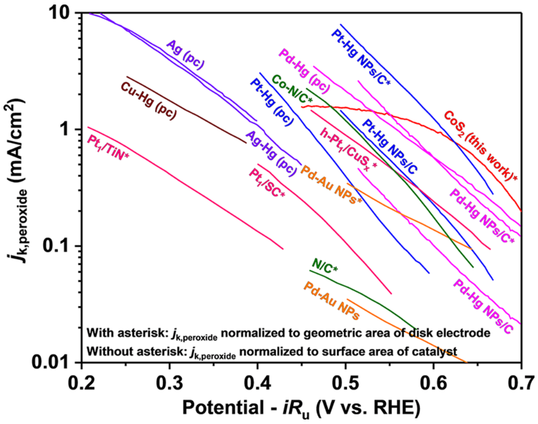

Figure 4. Comparisons of the mass-transport-corrected Tafel plots of the kinetic current densities for H_2O_2 production ($j_{k,peroxide}$, see definition in the Supporting Information) in the acidic solution for CoS_2 and other reported ORR electrocatalysts based on RRDE measurements. Data for CoS_2 (red trace) is from this work based on the RRDE voltammogram of drop-casted CoS_2 (cobalt loading = 305 $\mu g/cm_{disk}^2$) in 0.05 M H_2SO_4 at the rotation rate of 1600 rpm (shown in Figure 2a) and is cut-off at 0.45 V vs RHE where the ring current density (i.e., the hydrogen peroxide current density, $j_{peroxide}$, see definition in the Supporting Information) at 1600 rpm reaches its maximum. The curvature in data for CoS_2 is due to the decrease in the H_2O_2 selectivity of CoS_2 at higher overpotentials. Other data are adapted from the previous literature (as summarized in Table S3 in the Supporting Information): ref 14 for Pt−Au NPs; ref 15 for Pt−Hg NPs/C and Pt−Hg (pc); ref 16 for Pd−Hg NPs/C, Pd−Hg (pc), Ag (pc), Ag−Hg (pc), Cu−Hg (pc); ref 17 for Pt_1/SC; ref 18 for Pt_1/TiN; ref 19 for h-Pt_1/CuS_x; ref 36 for N/C; ref 37 for Co-N/C. The data with the asterisk (*) is normalized with the geometric area of the disk electrode. The data without the asterisk is normalized to the surface area of the catalyst (when available).

We further examined the operational stability of drop-casted CoS_2 by running successive RRDE scans in 0.05 M H_2SO_4 and 0.05 M Na_2SO_4 while sequentially changing the rotation rate back and forth between 400 and 2025 rpm (Figures S14 and S15). In both acidic and neutral solutions, the disk current density for the highest cobalt loading (305 $\mu g/cm_{disk}^2$) stayed almost unchanged over the scans (Figures S14d and S15d), suggesting that CoS_2 is reasonably stable under ORR conditions; on the other hand, the ring current density slightly decreased during operational stability tests (Figures S14e and S15e), which is likely due to the gradual poisoning of the Pt ring by the strongly absorbing sulfate anions from the electrolytes rather than the degradation of H_2O_2 selectivity (similar observations were also reported in a recent RRDE study of 2e$^-$ ORR on carbon materials in the strongly absorbing phosphate buffer solution[8]). At lower cobalt loadings, however, the decrease in the disk current density was more significant in both solutions (Figure S16). We further assessed the phase purity and surface chemical states of CoS_2 before and after operational stability tests with Raman spectroscopy and X-ray photoelectron spectroscopy (XPS). Raman spectra confirmed that the crystal structure of CoS_2 was well-preserved without the appearance of impurity phases after operational stability tests (Figure 5a). The binding energies of the predominant Co 2p (778.9 and 794.0 eV) and S 2p (163.0 and 164.0 eV) XPS signals, in good agreement with the literature values of pristine surface-unoxidized CoS_2,[21] remained the same after operational stability tests in both solutions (Figure 5b,c). We observed sulfate XPS signals (169.3 eV) after operational stability tests albeit their weak intensities. Although the sulfate peak might arise from sulfonate groups in the Nafion ionomer (we ruled out the possibility of the residual H_2SO_4 electrolyte in the tested catalyst by examining the catalysts tested in the $HClO_4$ electrolyte, see Figure S17), we suspect that the CoS_2 surface could be slowly oxidized into sulfate species by the dissolved O_2 or the electrogenerated H_2O_2 under ORR conditions and then be quickly refreshed to expose unoxidized CoS_2 upon the subsequent dissolution of sulfate species in both acidic and neutral solutions.

We also carried out the Koutecky−Levich (K−L) analysis as an alternative to determine the H_2O_2 selectivity (or the electron transfer number of the ORR). Since the K−L method requires a sufficient catalyst loading to completely react with the steady-state O_2 flux at the electrode surface and reach the limiting current,[30] we performed the K−L analysis on the highest catalyst loading of drop-casted CoS_2 in 0.05 M H_2SO_4. We used commercial Pt/C as an internal standard of the 4e$^-$ ORR in the acidic solution for the K−L analysis to deduce the electron transfer number of the ORR on drop-casted CoS_2 by comparing the slope of the K−L plots (Figure S18 and Table S4) to minimize the impact by the uncertainties in the diffusion constant of O_2 in the ionomer film and the kinematic parameters of the electrolyte. The K−L analysis (Figure S18c) yields similar (or slightly higher) H_2O_2 selectivity values of

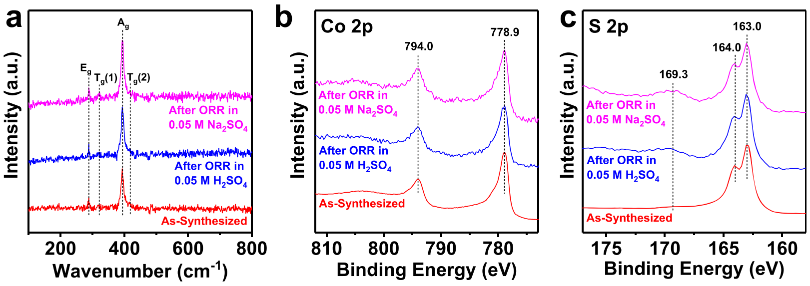

Figure 5. Structural and compositional characterizations of drop-casted CoS_2 before and after operational stability tests in O_2-saturated 0.05 M H_2SO_4 and 0.05 M Na_2SO_4. (a) Raman spectra, (b) Co 2p and (c) S 2p XPS spectra.

drop-casted CoS_2 and a similar trend up to about 0.46 V vs RHE compared with the RRDE method (Figure 2b); however, the H_2O_2 selectivity from the K−L method is clearly higher at the low overpotential region. We think that the RRDE method is better for the drop-casted CoS_2 electrode than the K−L method, because the K−L method is only applicable to single-step and one-way reactions with a first-order dependence on the gas-phase reactant, whereas the ORR is a multistep process with parallel pathways.[29,30] Therefore, we prefer to report the H_2O_2 selectivity determined by the RRDE method.

Finally, since RRDE only enables instantaneous detection of H_2O_2 intermediate, to ensure that H_2O_2 is indeed electrochemically produced on CoS_2 and can accumulate in the solution (which is critical for practical on-site production of H_2O_2), we carried out chemical, rather than electrochemical (RRDE), detection of H_2O_2 using a ceric sulfate titration method ($2Ce^{4+} + H_2O_2 \rightarrow 2Ce^{3+} + 2H^+ + O_2$).[8] To achieve a larger catalytic current and, therefore, a higher H_2O_2 yield, we directly grew CoS_2 nanowires onto the high-surface-area three-dimensional carbon fiber paper substrate as the working electrode (CoS_2/CFP, Figure 6a). A three-electrode H-cell setup (Figure S19) was used to avoid the oxidation of H_2O_2 product on the counter electrode, and a minimal volume (3 mL) of the electrolyte was filled into the working electrode compartment to obtain higher concentrations of H_2O_2. In 0.05 M H_2SO_4, the catalytic onset on CoS_2/CFP was similar to that on drop-casted CoS_2, whereas the plain CFP was inert toward the ORR (Figure S20). To perform the bulk ORR electrolysis on CoS_2/CFP in the acidic solution, we set the working electrode potential at 0.5 V vs RHE (around the optimal operating potential identified earlier from the RRDE results) and applied vigorous stirring (1200 rpm) to facilitate the mass transport of O_2 (Figure S20b). Two working electrodes with similar geometric areas (0.907 and 0.875 cm_{CFP}^2) fabricated from one synthesis of CoS_2/CFP (cobalt loading = ~374 μg/cm_{CFP}^2) were tested, showing highly reproducible results (Figures 6b and S21). During the 60 min bulk electrolysis, multiple aliquots of electrolyte were sampled out of the working electrode compartment at specific time intervals for chemical detection of H_2O_2 (Figure S22). Soon after the bulk electrolysis started, the overall catalytic current quickly reached steady state, the cumulative H_2O_2 yield displayed an almost linear increase for about 30 min (Figure 6c) with the cumulative H_2O_2 selectivity and Faradaic efficiency staying above 70 and 54% (Figure 6d, matched well with the RRDE results). As the bulk electrolysis further progressed, the overall catalytic current started to slowly increase, whereas the cumulative H_2O_2 yield experienced a less steady growth. We speculate that the accumulation of H_2O_2 in the electrolyte might speed up side reactions such as H_2O_2 reduction (generating additional current without increasing H_2O_2 yield) and/or decomposition (by the Nafion membrane or other impurities[15]). Nevertheless, at the end of the 60 min electrolysis, the cumulative H_2O_2 selectivity and Faradaic efficiency remained nearly 60 and 43%, respectively, and the cumulative H_2O_2 yield and concentration could eventually reach around 13 μmol and 148 mg/L, respectively. PXRD confirmed the crystalline phase of CoS_2 in the post-electrolysis CoS_2/CFP electrode (Figure S23). It is worth noting that there have been very few ORR catalysts reported with chemically quantified H_2O_2 production in acidic solutions, and most are based on noble metals.[15] The overall H_2O_2 production performance of CoS_2/CFP is comparable to that of the benchmark Pt−Hg alloy catalyst[15] under similar acidic conditions (see details in Table S5), making CoS_2 a more inexpensive and practical catalyst candidate for applications.

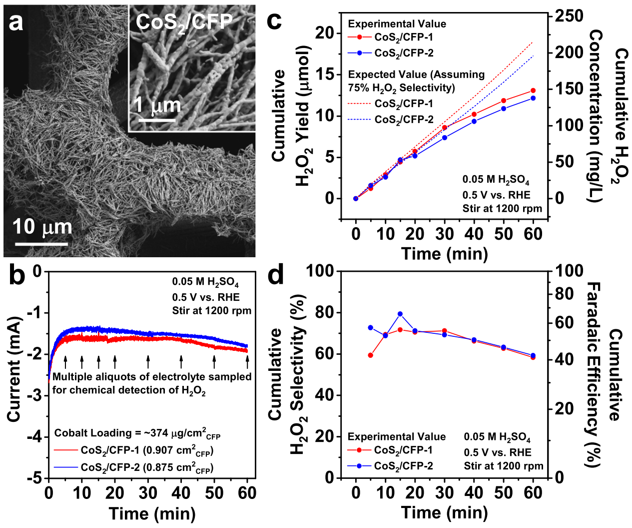

Figure 6. Electrocatalytic production of H_2O_2 on CoS_2/CFP in a three-electrode H-cell setup and chemical quantification of the H_2O_2 product. (a) SEM image of CoS_2/CFP. (b) Bulk ORR electrolysis of two CoS_2/CFP electrodes at 0.5 V vs RHE in O_2-saturated 0.05 M H_2SO_4 and the corresponding (c) cumulative H_2O_2 yield, (d) cumulative H_2O_2 selectivity and Faradaic efficiency.

■ CONCLUSIONS

In conclusion, our combined computational/experimental study demonstrates CoS_2 as an earth-abundant transition-metal compound showing great promise for electrocatalytic production of H_2O_2 in acidic and neutral solutions. Computations successfully predict the high activity and selectivity of CoS_2 toward $2e^-$ ORR due to the modest binding of OOH* adsorbate and the kinetically disfavored O−O bond scission resulting from its structural features. Both RRDE measurements of drop-casted CoS_2 nanomaterials and bulk ORR electrolysis using CoS_2 nanowires directly grown on the high-surface-area carbon fiber paper electrode followed by chemical quantification of H_2O_2 product show highly efficient electrocatalytic production of H_2O_2 on CoS_2 in the acidic solution (0.05 M H_2SO_4) with a ~70% H_2O_2 selectivity at ~0.5 V vs RHE and good operational stability. CoS_2 also catalyzes $2e^-$ ORR with less activity and selectivity in the noncorrosive neutral solution (0.05 M Na_2SO_4) that has practical implications. This integrated study, guided by computations, not only establishes an efficient and new earth-abundant electrocatalyst (CoS_2) for H_2O_2 production in acidic and neutral solutions but also reveals general mechanistic insights into the activity and selectivity of earth-abundant transition-metal compounds toward $2e^-$ ORR with unprecedented details, creating new opportunities in search of more active and selective electrocatalysts for highly efficient decentralized on-site production of H_2O_2.

■ METHODS AND MATERIALS

Computational Methods. All calculations were performed using the Vienna Ab-initio simulation package (VASP)[38−41] version 5.4.1 via the ASE interface.[42] Core electrons were treated using the projector augmented wave method[43,44] (valence electrons were expanded in plane waves up to 400 eV) in conjunction with the Perdew−Burke−Ernzerhof (PBE) exchange−correlation functional.[45,46] Single-point calculations were performed with the continuum solvent method VASPsol to account for solvation effects for surface-bound species.[47,48] The lattice constant of CoS_2 was determined by fitting to an equation of state,[49,50] with all atoms allowed to relax at a series of fixed lattice constants. The (100) surface of CoS_2 was modeled as a 1 × 1 slab with two repeats of the optimized primitive bulk unit cell in the direction perpendicular to the surface, yielding a thickness of 0.95 nm (a total of 8 Co atoms and 16 S atoms). Bulk calculations were performed using a Γ-centered 10 × 10 × 10 Monkhorst−Pack mesh,[51] whereas slab calculations used a 10 × 10 × 1 mesh. The bottom half of the slab was fixed to the bulk geometry, whereas the upper half was allowed to relax. Transition states were determined using the nudged elastic band and dimer routines and were confirmed to have one imaginary frequency corresponding to the reaction coordinate.[52−56] Vibrational frequencies for all calculations were determined by diagonalization of the mass-weighted partial Hessian (most earth-abundant isotopic masses) comprising all relaxed atoms.[57]

Binding free energies were calculated relative to $O_{2(g)}$ and $H_{(aq)}^+ + e_{(aq)}^-$. The free energy of $H_{(aq)}^+ + e_{(aq)}^-$ was determined at a given voltage relative to the standard hydrogen electrode via its equilibrium with $H_{2(g)}$ (the so-called computational hydrogen electrode).[22] To circumvent well-known issues with the DFT treatment of $O_{2(g)}$, its free energy was chosen to match the experimental reduction potential of $1/2O_2 + 2H^+ + 2e^- \rightarrow H_2O$ ($E^o = 1.229$ V). The free energies of all other species were determined by $G = H - TS^o$, where H is the enthalpy, including both zero-point and thermal enthalpy corrections, and S^o is the total experimental entropy at 298K and 1 bar (for gas-phase species) or calculated under the harmonic approximation (for surface-bound species). The free energy of liquid $H_2O_{(l)}$ was determined using the free energy of formation of liquid $H_2O_{(l)}$ and gas-phase $H_2O_{(g)}$. The solvation free energy of $H_2O_{2(aq)}$ was determined using the experimental Henry's law constant.[58] The calculated standard equilibrium reduction potential of the 2e⁻ ORR reaction $O_{2(g)} + 2H^+ + 2e^- \rightarrow H_2O_{2(aq)}$ is 0.81 V (as compared to the experimental value of 0.69 V).

In addition, energetics were also calculated with the PBE-D3(ABC) dispersion-corrected density functional method (Figure S1).[28] Although adding a dispersion correction caused adsorbed intermediates to bind more strongly to the CoS_2 surface, it led to an overall very small change in the energetics (compare Figures 1 and S1) and, therefore, did not affect the qualitative results.

Chemicals. All chemicals were used as received without any purification. Deionized nanopure water (Thermo Scientific, Barnstead Nanopure, 18.2 MΩ cm) was used for all experiments.

Materials Synthesis. The synthesis of CoS_2 nanomaterials and the direct growth of CoS_2 nanowires onto the carbon fiber paper substrate (CoS_2/CFP) follow a published procedure[21] with minor modifications (see the Supporting Information for details).

Materials Characterization. Powder X-ray diffraction (PXRD) patterns were collected on a Bruker D8 ADVANCE powder X-ray diffractometer using Cu Kα radiation. Scanning electron microscopy (SEM) and the corresponding energy dispersive X-ray spectroscopy (EDS) were performed on a Zeiss SUPRA 55VP field emission SEM equipped with a Thermo Fisher Scientific UltraDry EDS detector. The accelerating voltages for SEM and the corresponding EDS analyses were 1 and 17 kV, respectively. X-ray photoelectron spectroscopy (XPS) was performed on a Thermo Scientific K-Alpha XPS system with an Al Kα X-ray source. Raman spectroscopy was collected on a Horiba Labram Aramis Raman Spectrometer using a 532 nm laser source with attenuated laser intensity to avoid sample degradation. Detailed sample preparations for SEM, XPS, and Raman spectroscopy are described in the Supporting Information.

Electrode Preparation. All working electrodes for electrochemical measurements were prepared on a rotating ring-disk electrode (RRDE-3A, ALS Co., Ltd) comprised of a glassy carbon (GC) disk (O.D. 4 mm) surrounded by a Pt ring (I.D. 5 mm, O.D. 7 mm). The RRDE was polished successively with deagglomerated 1, 0.3, and 0.05 μm alumina suspensions (Allied High Tech Products, Inc.) on a polishing cloth (Buehler, MicroCloth, PSA), prewet with nanopure water, followed by rinsing thoroughly with nanopure water and methanol, sonicating in methanol for less than 20 s, and drying under ambient condition before use. To prepare working electrodes of drop-casted CoS_2 with the same Nafion loading but different cobalt loadings (Table S1), the same amount (~5 mg) of CoS_2 powders was suspended in different volumes of the 1:9 (v/v) mixture of the Nafion solution (Sigma-Aldrich, 5 wt % in lower aliphatic alcohols and water) and nanopure water by sonicating for 1 h, then a fixed volume (10 μL) of the suspension was drop-casted onto the disk of RRDE and dried under ambient condition at a rotation rate of 700 rpm to achieve a uniform catalyst film.[59]

Electrochemical Measurements. RRDE measurements were performed in a single-compartment three-electrode cell connected to two synchronized Bio-Logic SP-200 potentiostats. A graphite rod and a Hg/$HgSO_4$ (saturated K_2SO_4) electrode were used as the counter and reference electrodes, respectively. Solutions of 0.05 M H_2SO_4, 0.5 M H_2SO_4 (diluted from concentrated H_2SO_4, Sigma-Aldrich, 95.0−98.0%), and 0.1 M $HClO_4$ (diluted from concentrated $HClO_4$, Sigma-Aldrich, 70%, trace metal basis) were used as the acidic electrolyte; solution of 0.05 M Na_2SO_4 (prepared from Na_2SO_4, Sigma-Aldrich, ≥99.0%, anhydrous) was used as the neutral electrolyte. The pH values of as-prepared and O_2-saturated electrolytes (purged with O_2 gas for at least 15 min) were measured as follows.

pH = 1.26 for as-prepared 0.05 M H_2SO_4; pH = 1.26 for O_2-saturated 0.05 M H_2SO_4

pH = 5.71 for as-prepared 0.05 M Na_2SO_4; pH = 6.14 for O_2-saturated 0.05 M Na_2SO_4

pH = 1.02 for as-prepared 0.1 M $HClO_4$; pH = 0.35 for as-prepared 0.5 M H_2SO_4

The increase in the pH value after purging the electrolyte with O_2 gas was due to the elimination of dissolved CO_2 gas, which has a more pronounced effect on the neutral electrolyte compared with the acidic electrolyte. The Hg/$HgSO_4$ (saturated K_2SO_4) reference electrode was calibrated against the standard saturated calomel electrode (SCE, $E_{SCE} = 0.241$ V vs normal hydrogen electrode, NHE). Since the ORR measurements were performed in O_2-saturated electrolytes, all potentials were reported versus reversible hydrogen

DOI: 10.1021/acscatal.9b02546
ACS Catal. 2019, 9, 8433−8442

electrode (RHE) according to pH values of O_2-saturated electrolytes.

$E_{Hg/HgSO_4} = E_{SCE} + 0.404\ V = 0.645\ V$ vs NHE (in 0.05 M H_2SO_4)

E vs RHE = E vs NHE + 0.059×1.26 V = E vs Hg/$HgSO_4$ + 0.719 V (in 0.05 M H_2SO_4)

$E_{Hg/HgSO_4} = E_{SCE} + 0.409\ V = 0.650\ V$ vs NHE (in 0.1 M $HClO_4$)

E vs RHE = E vs NHE + 0.059×1.02 V = E vs Hg/$HgSO_4$ + 0.710 V (in 0.1 M $HClO_4$)

$E_{Hg/HgSO_4} = E_{SCE} + 0.434\ V = 0.675\ V$ vs NHE (in 0.5 M H_2SO_4)

E vs RHE = E vs NHE + 0.059×0.35 V = E vs Hg/$HgSO_4$ + 0.696 V (in 0.5 M H_2SO_4)

$E_{Hg/HgSO_4} = E_{SCE} + 0.383\ V = 0.624\ V$ vs NHE (in 0.05 M Na_2SO_4)

E vs RHE = E vs NHE + 0.059×6.14 V = E vs Hg/$HgSO_4$ + 0.986 V (in 0.05 M Na_2SO_4)

Detailed protocols for RRDE measurements are described in the Supporting Information.

Bulk ORR Electrolysis on Integrated CoS_2/CFP Electrode and Chemical Quantification of H_2O_2 Product. For bulk ORR electrolysis, CoS_2 nanowires directly grown on the carbon fiber paper (CoS_2/CFP) were used as the working electrode to achieve a larger catalytic current and, therefore, a higher H_2O_2 yield. To prepare working electrodes of CoS_2/CFP, 5 min epoxy (Devcon) was used to define the geometric area of the working electrodes to about 1 cm × 1 cm (Figure S19a). A three-electrode H-cell setup was used to avoid the oxidation of the H_2O_2 product on the counter electrode, and a minimal volume (3 mL) of the electrolyte was filled into the working electrode compartment to obtain higher concentrations of H_2O_2 (Figure S19b). Detailed protocols for bulk ORR electrolysis and chemical quantification of H_2O_2 product are described in the Supporting Information.

■ ASSOCIATED CONTENT

Ⓢ Supporting Information

The Supporting Information is available free of charge on the ACS Publications website at DOI: 10.1021/acscatal.9b02546.

> Supporting experimental methods on materials synthesis, materials characterization, and electrochemical measurement; supporting figures and tables on computational modeling, materials characterization, and electrochemical measurement (PDF)

■ AUTHOR INFORMATION

Corresponding Authors

*E-mail: schmidt@chem.wisc.edu. (J.R.S.).
*E-mail: jin@chem.wisc.edu. (S.J.).

ORCID

Hongyuan Sheng: 0000-0002-0494-4418
Diwen Ying: 0000-0002-6449-0649
Aurora N. Janes: 0000-0002-2916-5445
Wenjie Li: 0000-0001-9216-0922
J. R. Schmidt: 0000-0002-1438-117X
Song Jin: 0000-0001-8693-7010

Author Contributions

[‖]H.S., E.D.H, and X.Y. contributed equally to this work. H.S., X.Y., D.Y., and S.J. designed the experiments. H.S. carried out the synthesis, structural characterizations, RRDE measurements, ORR stability tests, and XPS analysis of CoS_2 nanomaterials presented here. H.S. directly grew CoS_2 nanowires on the carbon fiber paper electrode and performed bulk ORR electrolysis in an H-cell setup followed by chemical quantification of the H_2O_2 product. X.Y. and D.Y. performed the preliminary RRDE measurements of CoS_2 nanomaterials with the help of W.L. E.D.H., A.N.J., and J.R.S. conceived the computational modeling. E.D.H. performed the computational modeling with the help of A.N.J. D.Y. carried out the preliminary ORR study of CoS_2 films thermally sulfidized from electron-beam-evaporated cobalt films. H.S., E.D.H., X.Y., J.R.S., and S.J. wrote the manuscript and all of the authors commented on the manuscript.

Notes

The authors declare no competing financial interest.

■ ACKNOWLEDGMENTS

This research was partially supported by the National Science Foundation (NSF) Grant DMR-1508558 (H.S., W.L., and S.J.) for the material synthesis, by University of Wisconsin-Madison and King Abdullah University of Science and Technology (KAUST) OSR-2017-CRG6-3453.02 (H.S., W.L., and S.J.) for the electrochemical characterization, and CHE-1362136 (E.D.H, A.N.J., and J.R.S.) for the theoretical calculation. X.Y. and D.Y. thank the China Scholarship Council (CSC) and the National Natural Science Foundation of China (NSFC) Grant 51608319 for support. The authors gratefully acknowledge use of facilities and instrumentation supported by NSF through the University of Wisconsin Materials Research Science and Engineering Center (DMR-1720415).

■ REFERENCES

(1) Campos-Martin, J. M.; Blanco-Brieva, G.; Fierro, J. L. G. Hydrogen Peroxide Synthesis: An Outlook Beyond the Anthraquinone Process. *Angew. Chem., Int. Ed.* **2006**, *45*, 6962−6984.

(2) Yang, S.; Verdaguer-Casadevall, A.; Arnarson, L.; Silvioli, L.; Čolić, V.; Frydendal, R.; Rossmeisl, J.; Chorkendorff, I.; Stephens, I. E. L. Toward the Decentralized Electrochemical Production of H_2O_2: A Focus on the Catalysis. *ACS Catal.* **2018**, *8*, 4064−4081.

(3) Edwards, J. K.; Freakley, S. J.; Lewis, R. J.; Pritchard, J. C.; Hutchings, G. J. Advances in the Direct Synthesis of Hydrogen Peroxide from Hydrogen and Oxygen. *Catal. Today* **2015**, *248*, 3−9.

(4) Freakley, S. J.; He, Q.; Harrhy, J. H.; Lu, L.; Crole, D. A.; Morgan, D. J.; Ntainjua, E. N.; Edwards, J. K.; Carley, A. F.; Borisevich, A. Y.; Kiely, C. J.; Hutchings, G. J. Palladium-Tin Catalysts for the Direct Synthesis of H_2O_2 with High Selectivity. *Science* **2016**, *351*, 965−968.

(5) Wilson, N. M.; Pan, Y.-T.; Shao, Y.-T.; Zuo, J.-M.; Yang, H.; Flaherty, D. W. Direct Synthesis of H_2O_2 on AgPt Octahedra: The Importance of Ag−Pt Coordination for High H_2O_2 Selectivity. *ACS Catal.* **2018**, *8*, 2880−2889.

(6) Chu, S.; Cui, Y.; Liu, N. The Path Towards Sustainable Energy. *Nat. Mater.* **2017**, *16*, 16−22.

(7) Liu, Y.; Quan, X.; Fan, X.; Wang, H.; Chen, S. High-Yield Electrosynthesis of Hydrogen Peroxide from Oxygen Reduction by Hierarchically Porous Carbon. *Angew. Chem., Int. Ed.* **2015**, *54*, 6837−6841.

(8) Lu, Z.; Chen, G.; Siahrostami, S.; Chen, Z.; Liu, K.; Xie, J.; Liao, L.; Wu, T.; Lin, D.; Liu, Y.; Jaramillo, T. F.; Nørskov, J. K.; Cui, Y. High-Efficiency Oxygen Reduction to Hydrogen Peroxide Catalysed by Oxidized Carbon Materials. *Nat. Catal.* **2018**, *1*, 156−162.

(9) Chen, S.; Chen, Z.; Siahrostami, S.; Higgins, D.; Nordlund, D.; Sokaras, D.; Kim, T. R.; Liu, Y.; Yan, X.; Nilsson, E.; Sinclair, R.; Nørskov, J. K.; Jaramillo, T. F.; Bao, Z. Designing Boron Nitride

Islands in Carbon Materials for Efficient Electrochemical Synthesis of Hydrogen Peroxide. *J. Am. Chem. Soc.* **2018**, *140*, 7851−7859.

(10) Sa, Y. J.; Kim, J. H.; Joo, S. H. Active Edge-Site-Rich Carbon Nanocatalysts with Enhanced Electron Transfer for Efficient Electrochemical Hydrogen Peroxide Production. *Angew. Chem., Int. Ed.* **2019**, *58*, 1100−1105.

(11) Sun, Y.; Sinev, I.; Ju, W.; Bergmann, A.; Dresp, S.; Kühl, S.; Spöri, C.; Schmies, H.; Wang, H.; Bernsmeier, D.; Paul, B.; Schmack, R.; Kraehnert, R.; Roldan Cuenya, B.; Strasser, P. Efficient Electrochemical Hydrogen Peroxide Production from Molecular Oxygen on Nitrogen-Doped Mesoporous Carbon Catalysts. *ACS Catal.* **2018**, *8*, 2844−2856.

(12) Shi, X.; Zhang, Y.; Siahrostami, S.; Zheng, X. Light-Driven $BiVO_4$−C Fuel Cell with Simultaneous Production of H_2O_2. *Adv. Energy Mater.* **2018**, *8*, No. 1801158.

(13) Jirkovský, J. S.; Panas, I.; Ahlberg, E.; Halasa, M.; Romani, S.; Schiffrin, D. J. Single Atom Hot-Spots at Au−Pd Nanoalloys for Electrocatalytic H_2O_2 Production. *J. Am. Chem. Soc.* **2011**, *133*, 19432−19441.

(14) Pizzutilo, E.; Kasian, O.; Choi, C. H.; Cherevko, S.; Hutchings, G. J.; Mayrhofer, K. J. J.; Freakley, S. J. Electrocatalytic Synthesis of Hydrogen Peroxide on Au-Pd Nanoparticles: From Fundamentals to Continuous Production. *Chem. Phys. Lett.* **2017**, *683*, 436−442.

(15) Siahrostami, S.; Verdaguer-Casadevall, A.; Karamad, M.; Deiana, D.; Malacrida, P.; Wickman, B.; Escudero-Escribano, M.; Paoli, E. A.; Frydendal, R.; Hansen, T. W.; Chorkendorff, I.; Stephens, I. E. L.; Rossmeisl, J. Enabling Direct H_2O_2 Production through Rational Electrocatalyst Design. *Nat. Mater.* **2013**, *12*, 1137−1143.

(16) Verdaguer-Casadevall, A.; Deiana, D.; Karamad, M.; Siahrostami, S.; Malacrida, P.; Hansen, T. W.; Rossmeisl, J.; Chorkendorff, I.; Stephens, I. E. L. Trends in the Electrochemical Synthesis of H_2O_2: Enhancing Activity and Selectivity by Electrocatalytic Site Engineering. *Nano Lett.* **2014**, *14*, 1603−1608.

(17) Choi, C. H.; Kim, M.; Kwon, H. C.; Cho, S. J.; Yun, S.; Kim, H.-T.; Mayrhofer, K. J. J.; Kim, H.; Choi, M. Tuning Selectivity of Electrochemical Reactions by Atomically Dispersed Platinum Catalyst. *Nat. Commun.* **2016**, *7*, No. 10922.

(18) Yang, S.; Kim, J.; Tak, Y. J.; Soon, A.; Lee, H. Single-Atom Catalyst of Platinum Supported on Titanium Nitride for Selective Electrochemical Reactions. *Angew. Chem., Int. Ed.* **2016**, *55*, 2058−2062.

(19) Shen, R.; Chen, W.; Peng, Q.; Lu, S.; Zheng, L.; Cao, X.; Wang, Y.; Zhu, W.; Zhang, J.; Zhuang, Z.; Chen, C.; Wang, D.; Li, Y. High-Concentration Single Atomic Pt Sites on Hollow CuS_x for Selective O_2 Reduction to H_2O_2 in Acid Solution. *Chem* **2019**, *5*, 2099−2110.

(20) Faber, M. S.; Park, K.; Cabán-Acevedo, M.; Santra, P. K.; Jin, S. Earth-Abundant Cobalt Pyrite (CoS_2) Thin Film on Glass as a Robust, High-Performance Counter Electrode for Quantum Dot-Sensitized Solar Cells. *J. Phys. Chem. Lett.* **2013**, *4*, 1843−1849.

(21) Faber, M. S.; Dziedzic, R.; Lukowski, M. A.; Kaiser, N. S.; Ding, Q.; Jin, S. High-Performance Electrocatalysis Using Metallic Cobalt Pyrite (CoS_2) Micro- and Nanostructures. *J. Am. Chem. Soc.* **2014**, *136*, 10053−10061.

(22) Nørskov, J. K.; Rossmeisl, J.; Logadottir, A.; Lindqvist, L.; Kitchin, J. R.; Bligaard, T.; Jónsson, H. Origin of the Overpotential for Oxygen Reduction at a Fuel-Cell Cathode. *J. Phys. Chem. B* **2004**, *108*, 17886−17892.

(23) Viswanathan, V.; Hansen, H. A.; Rossmeisl, J.; Nørskov, J. K. Unifying the $2e^-$ and $4e^-$ Reduction of Oxygen on Metal Surfaces. *J. Phys. Chem. Lett.* **2012**, *3*, 2948−2951.

(24) Hansen, H. A.; Viswanathan, V.; Nørskov, J. K. Unifying Kinetic and Thermodynamic Analysis of 2 e^- and 4 e^- Reduction of Oxygen on Metal Surfaces. *J. Phys. Chem. C* **2014**, *118*, 6706−6718.

(25) Kulkarni, A.; Siahrostami, S.; Patel, A.; Nørskov, J. K. Understanding Catalytic Activity Trends in the Oxygen Reduction Reaction. *Chem. Rev.* **2018**, *118*, 2302−2312.

(26) Ford, D. C.; Nilekar, A. U.; Xu, Y.; Mavrikakis, M. Partial and Complete Reduction of O_2 by Hydrogen on Transition Metal Surfaces. *Surf. Sci.* **2010**, *604*, 1565−1575.

(27) Zhang, W.; Lai, W.; Cao, R. Energy-Related Small Molecule Activation Reactions: Oxygen Reduction and Hydrogen and Oxygen Evolution Reactions Catalyzed by Porphyrin- and Corrole-Based Systems. *Chem. Rev.* **2017**, *117*, 3717−3797.

(28) Grimme, S.; Antony, J.; Ehrlich, S.; Krieg, H. A Consistent and Accurate Ab Initio Parametrization of Density Functional Dispersion Correction (DFT-D) for the 94 Elements H-Pu. *J. Chem. Phys.* **2010**, *132*, No. 154104.

(29) Zhou, R.; Zheng, Y.; Jaroniec, M.; Qiao, S.-Z. Determination of the Electron Transfer Number for the Oxygen Reduction Reaction: From Theory to Experiment. *ACS Catal.* **2016**, *6*, 4720−4728.

(30) Wei, C.; Rao, R. R.; Peng, J.; Huang, B.; Stephens, I. E. L.; Risch, M.; Xu, Z. J.; Shao-Horn, Y. Recommended Practices and Benchmark Activity for Hydrogen and Oxygen Electrocatalysis in Water Splitting and Fuel Cells. *Adv. Mater.* **2019**, *31*, No. 1806296.

(31) Falkowski, J. M.; Concannon, N. M.; Yan, B.; Surendranath, Y. Heazlewoodite, Ni_3S_2: A Potent Catalyst for Oxygen Reduction to Water under Benign Conditions. *J. Am. Chem. Soc.* **2015**, *137*, 7978−7981.

(32) You, B.; Jiang, N.; Sheng, M.; Drisdell, W. S.; Yano, J.; Sun, Y. Bimetal−Organic Framework Self-Adjusted Synthesis of Support-Free Nonprecious Electrocatalysts for Efficient Oxygen Reduction. *ACS Catal.* **2015**, *5*, 7068−7076.

(33) Zhu, L.; Susac, D.; Teo, M.; Wong, K. C.; Wong, P. C.; Parsons, R. R.; Bizzotto, D.; Mitchell, K. A. R.; Campbell, S. A. Investigation of CoS_2-Based Thin Films as Model Catalysts for the Oxygen Reduction Reaction. *J. Catal.* **2008**, *258*, 235−242.

(34) Jirkovský, J. S.; Björling, A.; Ahlberg, E. Reduction of Oxygen on Dispersed Nanocrystalline CoS_2. *J. Phys. Chem. C* **2012**, *116*, 24436−24444.

(35) Jin, S. Are Metal Chalcogenides, Nitrides, and Phosphides Oxygen Evolution Catalysts or Bifunctional Catalysts? *ACS Energy Lett.* **2017**, *2*, 1937−1938.

(36) Hasché, F.; Oezaslan, M.; Strasser, P.; Fellinger, T.-P. Electrocatalytic Hydrogen Peroxide Formation on Mesoporous Non-Metal Nitrogen-Doped Carbon Catalyst. *J. Energy Chem.* **2016**, *25*, 251−257.

(37) Yamanaka, I.; Ichihashi, R.; Iwasaki, T.; Nishimura, N.; Murayama, T.; Ueda, W.; Takenaka, S. Electrocatalysis of Heat-Treated Cobalt-Porphyrin/Carbon for Hydrogen Peroxide Formation. *Electrochim. Acta* **2013**, *108*, 321−329.

(38) Kresse, G.; Hafner, J. Ab Initio Molecular Dynamics for Liquid Metals. *Phys. Rev. B* **1993**, *47*, 558−561.

(39) Kresse, G.; Hafner, J. Ab Initio Molecular-Dynamics Simulation of the Liquid-Metal–Amorphous-Semiconductor Transition in Germanium. *Phys. Rev. B* **1994**, *49*, 14251−14269.

(40) Kresse, G.; Furthmüller, J. Efficient Iterative Schemes for Ab Initio Total-Energy Calculations Using a Plane-Wave Basis Set. *Phys. Rev. B* **1996**, *54*, 11169−11186.

(41) Kresse, G.; Furthmüller, J. Efficiency of Ab-Initio Total Energy Calculations for Metals and Semiconductors Using a Plane-Wave Basis Set. *Comput. Mater. Sci.* **1996**, *6*, 15−50.

(42) Bahn, S. R.; Jacobsen, K. W. An Object-Oriented Scripting Interface to a Legacy Electronic Structure Code. *Comput. Sci. Eng.* **2002**, *4*, 56−66.

(43) Blöchl, P. E. Projector Augmented-Wave Method. *Phys. Rev. B* **1994**, *50*, 17953−17979.

(44) Kresse, G.; Joubert, D. From Ultrasoft Pseudopotentials to the Projector Augmented-Wave Method. *Phys. Rev. B* **1999**, *59*, 1758−1775.

(45) Perdew, J. P.; Burke, K.; Ernzerhof, M. Generalized Gradient Approximation Made Simple. *Phys. Rev. Lett.* **1996**, *77*, 3865−3868.

(46) Perdew, J. P.; Burke, K.; Ernzerhof, M. Generalized Gradient Approximation Made Simple [Phys. Rev. Lett. 77, 3865 (1996)]. *Phys. Rev. Lett.* **1997**, *78*, No. 1396.

(47) Mathew, K.; Sundararaman, R.; Letchworth-Weaver, K.; Arias, T. A.; Hennig, R. G. Implicit Solvation Model for Density-Functional Study of Nanocrystal Surfaces and Reaction Pathways. *J. Chem. Phys.* **2014**, *140*, No. 084106.

(48) Mathew, K.; Hennig, R. G. Implicit Self-Consistent Description of Electrolyte in Plane-Wave Density-Functional Theory, arXiv:1601.03346. arXiv.org e-Print archive. https://arxiv.org/abs/1601.03346 (accessed Jun 12, 2019).

(49) Alchagirov, A. B.; Perdew, J. P.; Boettger, J. C.; Albers, R. C.; Fiolhais, C. Energy and Pressure Versus Volume: Equations of State Motivated by the Stabilized Jellium Model. *Phys. Rev. B* **2001**, *63*, No. 224115.

(50) Alchagirov, A. B.; Perdew, J. P.; Boettger, J. C.; Albers, R. C.; Fiolhais, C. Reply to "Comment on 'Energy and Pressure Versus Volume: Equations of State Motivated by the Stabilized Jellium Model' ". *Phys. Rev. B* **2003**, *67*, No. 026103.

(51) Monkhorst, H. J.; Pack, J. D. Special Points for Brillouin-Zone Integrations. *Phys. Rev. B* **1976**, *13*, 5188−5192.

(52) Henkelman, G.; Jónsson, H. Improved Tangent Estimate in the Nudged Elastic Band Method for Finding Minimum Energy Paths and Saddle Points. *J. Chem. Phys.* **2000**, *113*, 9978−9985.

(53) Jónsson, H.; Mills, G.; Jacobsen, K. W. Nudged Elastic Band Method for Finding Minimum Energy Paths of Transitions. In *Classical and Quantum Dynamics in Condensed Phase Simulations*; Berne, B. J., Ciccotti, G., Coker, D. F., Eds.; World Scientific, 1998; pp 385−404.

(54) Henkelman, G.; Jónsson, H. A Dimer Method for Finding Saddle Points on High Dimensional Potential Surfaces Using Only First Derivatives. *J. Chem. Phys.* **1999**, *111*, 7010−7022.

(55) Heyden, A.; Bell, A. T.; Keil, F. J. Efficient Methods for Finding Transition States in Chemical Reactions: Comparison of Improved Dimer Method and Partitioned Rational Function Optimization Method. *J. Chem. Phys.* **2005**, *123*, No. 224101.

(56) Kästner, J.; Sherwood, P. Superlinearly Converging Dimer Method for Transition State Search. *J. Chem. Phys.* **2008**, *128*, No. 014106.

(57) Cohen, E. R.; Cvitas, T.; Frey, J. G.; Holström, B.; Kuchitsu, K.; Marquardt, R.; Mills, I.; Pavese, F.; Quack, M.; Stohner, J.; Strauss, H. L.; Takami, M.; Thor, A. J. *Quantities, Units and Symbols in Physical Chemistry*, 3rd ed.; IUPAC & RSC Publishing, 2007.

(58) NIST Chemistry Webbook. https://webbook.nist.gov/cgi/cbook.cgi?ID=C7722841&Mask=10#Solubility (accessed Jun 12, 2019).

(59) Garsany, Y.; Singer, I. L.; Swider-Lyons, K. E. Impact of Film Drying Procedures on RDE Characterization of Pt/VC Electrocatalysts. *J. Electroanal. Chem.* **2011**, *662*, 396−406.

■ NOTE ADDED AFTER ASAP PUBLICATION

This paper originally published ASAP on August 15, 2019. Figures 3 and 4 were replaced, and the corrected version was reposted on August 16, 2019.